batteries

MDPI

Article

Design and Simulations of RT Na-S Battery/Supercapacitor Energy Storage Systems Integrated in Grid/Microgrid with Renewables

Hakeem Ademola Adeoye , Mona Elghzal and Constantina Lekakou *

School of Engineering, University of Surrey, Guildford GU2 7XH, UK; h.adeoye@surrey.ac.uk (H.A.A.)
* Correspondence: c.lekakou@surrey.ac.uk

Abstract

A sustainable non-lithium battery is proposed, integrated with renewables to cater for the intermittency and differences between daily supply and demand. A room temperature sodium–sulfur (RT Na-S) battery presented in this study offers a promising energy density of 177 Wh/kg of the pouch cell. A framework is introduced for the design of an RT Na-S battery system, alone and combined with a supercapacitor, and its operating schedule for two case studies: (a) a photovoltaic (PV) system for a household and (b) a wind turbine for an industrial site. Daily power supply and demand profiles are included in both cases. In the first design step, the required mass and volume of the battery cells are determined. In the second step, the system architecture is designed, and simulations of the renewable-energy storage system–demand are carried out for four consecutive days. An RT Na-S battery–supercapacitor system is recommended in association with the wind turbine that involves high frequency and high power pulses, where the supercapacitor caters for power exceeding 0.1 C. A standalone RT Na-S battery is recommended for the PV system. The simulations predicted that each storage system covered all the net power and energy demands without any contributions from the grid.

Keywords: RT Na-S battery; supercapacitor; PV panel system; wind turbine system; design; simulations; equivalent electric circuit model

Academic Editor: Paul Arévalo

Received: 28 August 2025
Revised: 3 November 2025
Accepted: 4 November 2025
Published: 5 November 2025

Citation: Adeoye, H.A.; Elghzal, M.; Lekakou, C. Design and Simulations of RT Na-S Battery/Supercapacitor Energy Storage Systems Integrated in Grid/Microgrid with Renewables. *Batteries* **2025**, *11*, 409. https://doi.org/10.3390/batteries11110409

1. Introduction

Given the intermittent nature of renewables, with the focus on wind and photovoltaic energy, energy storage systems are urgently needed to cover differences between supply and demand during the day and interseasonally [1–5]. European statistics reported that in September 2024, Europe had 278 GW of wind power capacity, with 243 GW onshore and 35 GW offshore, where Europe was defined to include all European countries including those within and outside the European Union (EU) [6]. Furthermore, a capacity of 333 GW of solar energy devices or panels was reported for 2024 within EU [7]. Apart from daily and interseasonal variations, there is also large variation between countries [8–12]: energy storage systems will also smooth the geographical distribution of the produced electric energy as per needs of demand and agreements between distributors, regions and countries.

Amongst the different types of energy storage, electrochemical energy storage has the highest efficiency: 80–90% for Li-ion batteries [13–24], 88% for a pouch cell of room temperature (RT) sodiated hard carbon anode and sulfur cathode [25], 70–80% for selected low overpotential RT Na-S batteries [26–30] and 95–100% for supercapacitors [31–50]. Other types of energy storage techniques include the following: gravitational energy storage (GES) with an efficiency of 95–97% for cases where natural water heads exist (e.g., hydropower plant in Kremasta, Greece, at 96.7% efficiency [51–56]) and 72–75% efficiency for GES with induced "charge"—"discharge" phases realized by pumped hydropower electricity storage (PHES) [57–62]. Compressed air energy storage (CAES) exhibits even lower efficiency of 42–54% that might be raised to 70–80% if the lost heat during compression is utilized [63–68]. Thermal energy storage also has low energy efficiency of 50–70% [69–74].

Average wind speeds around the UK coast and North Sea coast of Ireland, Germany, Denmark, Netherlands and Belgium have been reported to be above 8 m s^{-1}, above 9 m s^{-1} in open sea [75–80], and above 11 m s^{-1} on hills and ridges [81–85], where wind power fluctuations of the order of 700 W m^{-2} have been reported [86–91]. For an electrochemical energy storage system, it is possible that a battery–supercapacitor system may be more suitable to cater for rapid wind power fluctuations, and this is included in the present feasibility study. However, the widespread use of Li-ion batteries in the electrification of different sectors raises the question about whether the oil-dependent economy will be replaced by a lithium and rare materials-dependent economy. Furthermore, the different types of Li-ion batteries extensively use many critical raw materials (CRMs), such as elements Li, Ni, Mn, Co and Ti. Intensive research within our group focuses on non-lithium sulfur batteries and sodium–sulfur (Na-S) batteries, in which lithium is replaced by sodium in the anode and Li, Ni, Mn and Co are replaced by sulfur in the cathode.

Room-temperature sodium–sulfur (RT Na-S) batteries offer a valid alternative to Li-ion batteries, as they are based on the abundant materials sodium and sulfur, of which sulfur offers high theoretical capacity [92,93]. Intensive research in the last decade has led to the development of cathode hosts that prevent the shuttling of polysulphides in sulfur batteries with liquid electrolytes [94–100]. High-temperature (HT) Na-S batteries are available commercially, operating at 300–340 °C, and are used for stationary energy storage with renewables [101–103]. However, the elevated temperatures raise fire and explosion risks [104–108].

Further developments yielded sodium salts soluble in organic solvents [109–114] which enabled RT Na-S batteries. Examples include an RT Na-S coin cell of 25 wt% S in an activated carbon fabric cathode host and electrolyte 1.5 M $NaClO_4$ and 0.2 M $NaNO_3$ in TEGDME at electrolyte/sulfur ratio E/S = 10.4 μL/mg_S, which reached 360 Wh/$kg_{cathode+Na}$ at 0.2 C after 700 cycles [115]; and an RT Na-S pouch cell of 10 cell layers with 45 wt% S in a hollow porous particle Ketjenblack-based cathode [25,116], sodiated hard carbon anode, and electrolyte 1 M $NaClO_4$, 0.1 M Na_2S and 0.1 M P_2S_5 in TEGDME at E/S = 13 μL/mg_S that reached an estimated optimized gravimetric and volumetric energy density of 109 Wh/kg_{cell} and 164 Wh/L_{cell}, respectively, in discharge at 0.1 C tested to 1000 cycles with 88.6% energy efficiency [25]. Such energy densities are comparable, or even better, than the volumetric and gravimetric energy density of second-life LFP batteries which are sufficiently old to be recycled from electric vehicles (EVs) to grid applications nowadays [117–122]. Although cycling of RT Na-S batteries at higher rates has been reported, the risk of dendrite formation in batteries with metal anodes has led to the decision to restrict the operation of RT Na-S batteries in this study at 0.1 C for safety reasons. Given that the recommended charge rate even for new LFP batteries is 0.1 C, such a low rate has been considered reasonable to set as the limit in the present study. Higher C-rates could be achieved for RT Na-S batteries with a sodiated hard carbon anode so that there is no risk of dendrite formation: a study with a 10-layer pouch cell was tested at 0.2 C up to 1000 cycles [25]. The first task of the present study is to finetune an RT Na-S battery to raise its energy density while maintaining low C-rates in the range of

0.1–0.2 C to avoid dendrite formation. Our group has great experience in eliminating the sulfur and sulfide "shuttling" phenomenon in Li-S batteries via the following techniques which shall be investigated for the cathodes of the RT Na-S battery in this study: (a) the use of hollow porous carbon particles as cathode hosts [25,95,123]; (b) employing PEDOT:PSS as a cathode binder [95,124]; and (c) spraying a thin B,N doped graphene nanoplatelet (BNG) interlayer on the cathode surface [95]. Initial trials with such novel cathodes in RT Na-S cells employing a two-part rigid cell case [14,125] within our group indicated that the high cathode expansion at high specific capacity leads to cracks and fragmentation in the cathode which raises the cell resistance and leads to the deterioration of the battery performance. Hence, we are proposing the fabrication and testing of scaled up RT Na-S pouch cells in this study which would allow better cathode expansion and minimize the amount of required electrolyte [32,126].

The combination of the RT Na-S battery with a supercapacitor may increase the C-rate of the system [125,127,128]. Supercapacitors feature high power density but low energy density and a long lifetime [34,129]. Both supercapacitors and RT Na-S batteries can also be easily recycled via solvent-aided processing [130].

Hence, this study offers novel contributions in a number of areas regarding high energy storage batteries without critical raw materials and the design and simulations of hybrid energy storage systems integrated with renewables.

(a) By employing abundant sodium and sulfur materials for the anode and cathode, respectively, which avoids the dependence of Li-ion batteries on lithium and rare cathode materials, the latest advances in RT Na-S batteries are adopted in an RT Na-S battery pouch cell finetuned in this study. The electrochemical test data for this innovative RT Na-S battery pouch cell are presented and employed in the energy storage systems designed and simulated in this study.
(b) The framework is set for the preliminary and in-depth design of energy storage systems based on RT Na-S batteries and supercapacitors, according to needs, integrated with microgrid or grid with solar and wind energy renewables. The contributions are important in the RT Na-S battery sizing and simulations.
(c) Simulations are conducted for systems designed for two case studies, featuring a PV panel system for a household and a wind turbine for an industrial site, respectively. Studying the simulation results leads to improvements in the design of the energy storage system and its operating conditions. The innovation lies in the scenario-specific system optimization (standalone RT Na-S for PV, hybrid system for high-frequency wind power pulses).

2. Specifications of Use Cases with Solar and Wind Energy Renewables

The first step in the design framework is to assemble the specifications of the grid/microgrid usage and the specifications of each of its components. Starting with renewables, two use cases of renewables are covered for individual units: a PV system for a household integrated with the grid (or a microgrid), and a wind turbine for an industrial site also integrated with the grid. Figure 1 presents the power profiles of supply and demand for each of the two types of renewables considered in this study. Figure 1a depicts the example of a system of 10 m^2 PV of 20% efficiency, an average maximum power profile based on the PV energy produced from the corresponding solar irradiation profile in the most sunlit month of the year, July, in Athens, so that a high-capacity energy storage system is specified. In general, although fluctuations of solar irradiation might occur on cloudy days, the power does not exceed the maximum profile of a sunny day in July [131,132]. Figure 1a also displays a representative electricity load profile for a household [133]. Profiles integration yields a daily PV energy supply of 14,650 Wh and daily electric energy demand of 11,376 Wh. The overlap area between the PV supply and demand profiles represents the electric energy covered directly by the PV. The blue areas under the demand profile above and outside the PV profile, early in the morning and late in the evening, represent the energy supplied directly from the grid to cover the demand or the energy supplied from the battery to cover the demand if the battery SoC is greater than 0. From 10.4 to 18.7 h, the PV directly supplies 2915 Wh to cover the electricity demand of the household and may store the rest of the PV energy in the energy storage system, which amounts to 9985 Wh. From the PV and demand profiles in Figure 1a, it is also determined that the maximum power of charging the battery reaches 1651 W. Given possible fluctuations of the demand profile that, within the energy storage period, might be switched off at times, the maximum specified charge power of the battery in Figure 1a is increased to 1830 W, i.e., the maximum PV power.

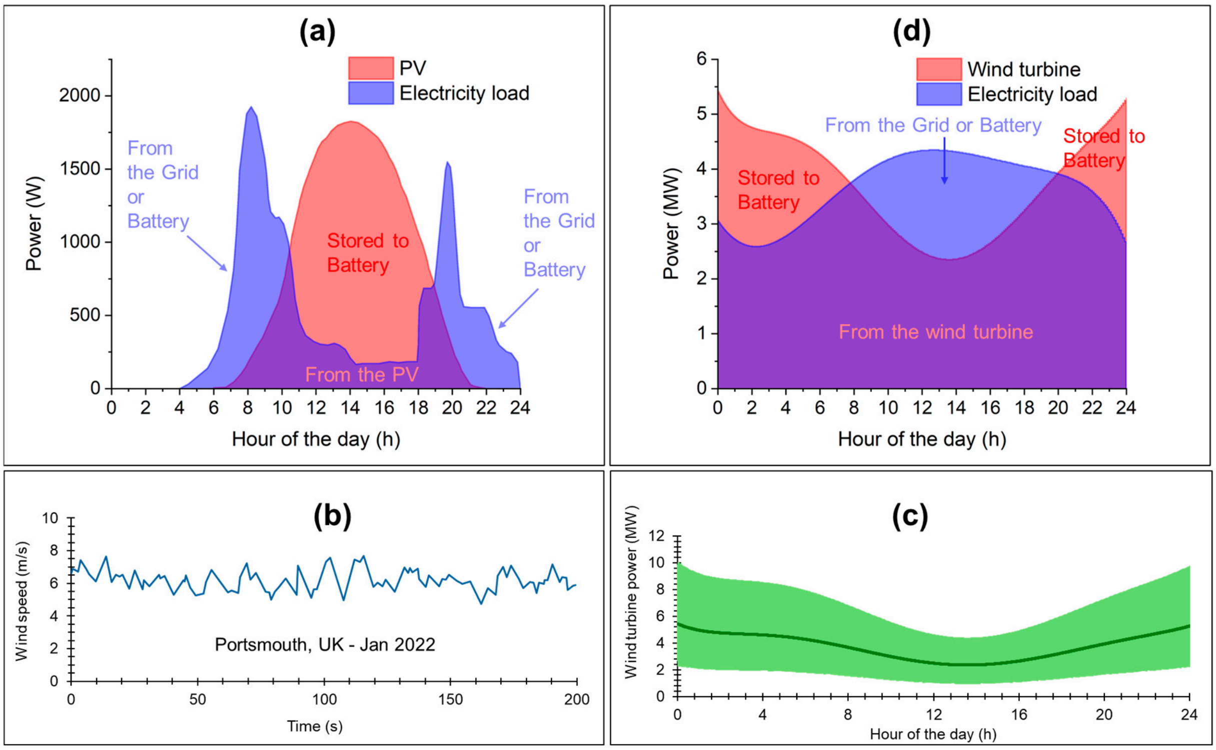

Figure 1. Supply and demand power profiles for a PV and a wind turbine. (**a**) Daily average PV power profile in Athens (based on daily solar irradiation in July—maximum in the year from data in [132]) and load demand profile [133] assumed by a household. (**b**) Wind speed data measured in January in Portsmouth (UK) in this study. (**c**) Daily wind turbine profile adjusted with fluctuations following wind speed fluctuations in (**b**). (**d**) Daily average wind turbine power profile in January in Portsmouth (UK) against the load demand profile assumed for an industrial site.

Figure 1b presents fluctuating wind data in Portsmouth, UK, in January, one of the highest wind speed months there. The data was obtained for this study with a CALYPSO ultrasonic portable mini wind meter at a sample rate frequency of 1 Hz and resolution of 0.1 m s^{-1}. Considering a wind turbine of blade length L = 100 m, the wind speed data (n) is translated to wind turbine power data presented in Figure 1c, using the equation for the theoretical wind turbine power, P_{WT} [134]:

$$P_{WT} = \frac{8}{27}\rho_a \pi L^2 v^3 \quad (1)$$

where ρ_a is the air density. The wind turbine power data in Figure 1c consists of an average profile and fluctuations generated from the ratio of wind fluctuations with respect to the average wind speed in the wind speed profile sample presented in Figure 1b. Figure 1d presents the average daily profile of the wind turbine power against the daily electricity demand of an industrial site near which the wind turbine is installed. The overlap area between the wind turbine supply and demand profiles in Figure 1d represents the electric energy covered directly by the wind turbine. The blue area under the demand profile and above the wind power profile, between 7.78 h and 19.96 h, represents the energy supplied directly from the grid to cover the demand or supplied from the battery if the battery SoC is greater than 0. From 19.96 h to 24 h and from 0 h to 7.78 h of the following day, the wind turbine has an excess energy of 16,802 kWh that may be stored in a battery. From the wind power and demand profiles in Figure 1d, taking also the fluctuating profile in Figure 1c, it is also determined that the maximum power of charging the battery reaches 7.133 MW and the maximum discharge power may reach 3.319 MW.

Hence, two different energy storage systems need be designed in this study: (i) An energy storage system for the household PV with an energy capacity of 9985 Wh, a maximum charge power of 1830 W and a maximum discharge power of 1926 W. (ii) An energy storage system for the industrial site wind turbine with an energy capacity of 16,802 kWh, a maximum charge power of 7133 kW and a maximum discharge power of 3319 kW.

3. RT Na-S Battery

3.1. Materials and Experimental Methods

A 100 mm × 100 mm monolayer pouch cell was fabricated comprising the following: a cathode coating of 50 wt% sulfur (Sigma Aldrich, Gillingham, UK), 40.5 wt% KJB (Ketjenblack EC-600JD, Lion Corp., Tokyo, Japan) and 9.5 wt% PEDOT:PSS (Heraeus, Hanau, Germany) on carbon-coated aluminum current collector (MTI Corp., Richmond, CA, USA) fabricated as described in [95]; a thin BNG (Graphitene, Scunthorpe, UK) interlayer sprayed on the cathode; about 0.1 mm-thick Na foil anode in-house fabricated via rolling; separator Celgard® 2400; electrolyte 1M NaTFSI (Solvionic, Toulouse, France), 0.3 M $NaNO_3$ and 0.8 wt% gelatin in TEGDME (Sigma Aldrich, UK) at optimized E/S = 6 μL/mg_S. Table 1 presents the mass composition of a 10-layer pouch cell of RT Na-S battery, extrapolated from the composition of the monolayer pouch cell of this study. The 10-layer pouch cell is in a parallel layer cell connection and comprises double-side coated cathode current collectors and Na anode foil shared between adjacent layer cells [32,34].

Table 1. Mass Composition of a 10-layer pouch cell of RT Na-S battery.

Component	Weight%
Sulfur	6.76
Cathode total (incl. sulfur)	13.52
Current collector foil	1.13
Na foil	14.54
Electrolyte	40.94
Separator	1.69
Tags	11.27
Pouch material	16.91
TOTAL	100.00

3.2. Experimental Results of Cycled RT Na-S Pouch Cell

Figure 2a displays the galvanostatic dischage–charge (GDC) curves of the novel RT Na-S pouch cell described in Section 3.1, which achieved 1400 mAh/g_S in discharge at 0.1 C after 200 cycles, with this capacity value at discharge stabilized in the last 10 tested cycles at 0.1 C. On the basis of these GDC curves and the composition of a multilayer pouch cell presented in Table 1, a gravimetric and volumetric energy density of 177 Wh/kg_{cell} and 287 Wh/L_{cell}, respectively, was estimated in discharge at 0.1 C. The pouch cell exhibits 75% energy efficiency due to the high overpotential creating a large potential difference between charge and discharge, although the cell in Figure 2a has the advantage of offering a long potential plateau compared to other RT Na-S technologies with different electrolyte systems ([25]: 109 Wh/kg_{cell} and 164 Wh/L_{cell}). In terms of power density, 0.1 C-rate is translated to an average of 22.7 W/kg_{cell} and 36.6 W/L_{cell} in charge, and 17.7 W/kg_{cell} and 28.6 W/L_{cell} in discharge.

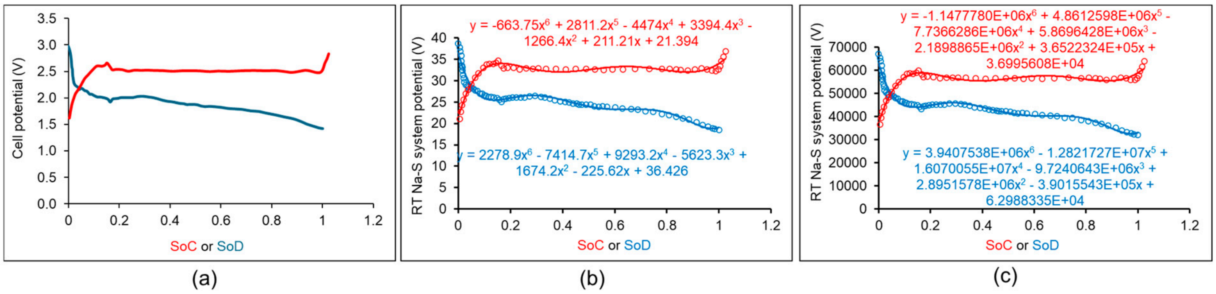

Figure 2. Galvanostatic discharge–charge curves at 0.1 C: (**a**) RT Na-S cell fabricated and tested for this study with a discharge capacity of 1400 mAh/g_S; (**b**) RT Na-S battery system designed for the PV system with a discharge capacity of 416 Ah; (**c**) RT Na-S battery system designed for the wind turbine system with a discharge capacity of 400 Ah.

HT Na-S batteries offer higher energy densities of up to 200 Wh/kg_{cell} [135] but operate at high temperatures of 300–340 °C [101–103] which pose a fire and explosion risk. Due to the novelty of RT Na-S batteries, there is a lack of scaled-up cell data and, hence, energy density data with respect to cell mass rather than electrode or just sulfur mass. Our RT Na-S battery cell has higher energy density than that of the RT sodiated hard carbon-sulfur cell of Pampel et al. [25], which may be attributed to the lower E/S ratio of our cell and the additional hard carbon mass in the anode of their cell. Sodium-ion (Na-ion) batteries are another non-lithium battery technology still under development, with the French research agency CNRS CEA having launched a commercial 18,650 cylindrical cell of 90 Wh/kg_{cell} and 250 Wh/L_{cell} [136], whereas other Na-ion cells reported in the literature with cathodes rich in critical raw materials exhibited higher energy densities of 150 Wh/kg for a $NaNi_{0.68}Mn_{0.22}Co_{0.10}O_2$ cathode or a $Na_3V_2(PO_4)_2F_3$ cathode [136]. Our RT Na-S battery for energy storage integrated with renewables may also be compared to safe Li-ion batteries with reduced CRM content, such as $LiFePO_4$ (LFP) batteries. Typical LFP batteries (commercially available as new or second-life batteries [117–122]) offer an energy density of 90–160 Wh/kg or 150–Wh/L [117–122,137–139], rising to 180 Wh/kg for state-of-the-art LFP cells [140], and a power density of 2000 W/kg in discharge [140] but much lower in charge at 100–200 W/kg [141].

On the basis of this data for the RT Na-S battery cell, a preliminary design is conducted to cover the mean power and energy requirements of the PV and wind turbine renewables presented in Figure 1a,b, respectively. An amount of 57 kg or 35 L of RT Na-S battery cells are required to store and deliver 9985 Wh of PV energy (also taking into account 75% energy efficiency of our RT Na-S battery cells), which, at an average of 22.7 W/kg_{cell} and 36.6 W/L_{cell} in charge, cannot fully satisfy the maximum charge power requirement of 1830 W. At 17.7 W/kg_{cell} and 28.6 W/L_{cell} in discharge, 57 kg or 35 L of RT Na-S battery cells cannot satisfy the maximum discharge power requirement of 1926 W (Figure 1a). Hence, a total of 109 kg or 67 L of RT Na-S battery (i.e., an extra 52 kg or 32 L of battery) is needed to cover the maximum power in discharge, which seems to be the controlling factor in this case, which also covers the maximum power in discharge and can cater to the total energy requirement in both charge and discharge; in fact, it can store and deliver an extra of 9308 Wh. Alternatively, if only 57 kg or 35 L of RT Na-S battery is used to cover the energy storage requirement, 1293.9 W charge power and 1008.9 W discharge power, then 155 kg of a high energy density supercapacitor (10 Wh kg^{-1} and power density of 1750 W kg^{-1} in charge and discharge [32,34]) could be used to cover the extra 1550 Wh at a power above 1293.9 W in charge and 1470 Wh at a power above 1008.9 W in discharge. Clearly, the lowest mass option is a total mass of 109 kg or 67 L of RT Na-S battery mass which can cover all the energy and power requirements of Figure 1a.

A preliminary design of the RT Na-S battery is also conducted to cover the mean power and energy requirements of the wind turbine renewable and load presented in Figure 1d. A total of 95 tons or 58.5 m^3 of RT Na-S battery cells are required to store and deliver 16,802 kWh of wind turbine energy (also taking into account 75% energy efficiency of our RT Na-S battery cells), which at an average of 22.7 W/kg_{cell} cover only 2.157 MW out of the 7.133 MW required in charge, and at an average of 17.7 W/kg_{cell} cover only 1.6815 MW out of the 3.319 MW required in discharge. An extra mass of 220 tons of RT Na-S battery cells is required to cover the extra power required. Alternatively, 84.11 tons or 96.1 m^3 of a high energy density supercapacitor (10 Wh kg^{-1} and power density of 1750 W kg^{-1} [32,34]) is needed to cover 0.31 MWh at powers above 2.157 MW in charge and 0.8411 MWh at powers above 1681.5 kW in discharge. In conclusion, the lowest mass option is a total amount of 179.11 tons or 154.6 m^3 of RT Na-S battery and supercapacitor cells that can cover all the energy and power requirements of Figure 1d.

4. Design and Simulations of Energy Storage Systems for Solar and Wind Energy Renewables

4.1. Design and Simulations of Energy Storage System Integrated with PV System

The PV system for Figure 1a is considered to be 10 m^2 of 10 PV panels with a maximum power of 200 W each, in 2p5s connection as presented in Figure 3, with a nominal PV system potential of 24 V, maximum potential of 38 V, and maximum power of 2 kW. The system is connected in parallel with an RT Na-S battery pack of 13 modules in series with a maximum potential of 3 V per module (to be charged to a maximum of 39 V) and an average potential of 1.87 V per module (system voltage of 24.31 V on average). For the battery system to store 9985 Wh at a nominal system voltage of 24 V, each module needs to be of 416 Ah, with the characteristic discharge–charge curves of the RT Na-S battery system at 0.1 C and the related polynomials fitted to the experimental data presented in Figure 2b. Considering a battery cell of 59 Ah (which is an assumed scaled-up version of our cell presented in Section 3.2 and Figure 2a, with the same specific capacity, energy density, power density in charge and discharge and energy efficiency), seven such cells need to be connected in parallel to form a battery module. As presented in Figure 3, a DC/DC converter is connected between the PV and the battery system to control the voltage within the limits of each system, and a DC/AC converter is connected between the PV and the AC grid connected with the house.

The battery system is modeled by an equivalent circuit model (ECM) as presented in Figure 3, which consists of an in-series resistance R0 = 2.75 m-ohm, a Voigt element of a capacitor C1 = 157.8 F and a resistor R1 = 3.4 m-ohm (from electrical impedance spectroscopy data of our RT Na-S pouch cell presented in Section 3.2 after 200 cycles at 0.1 C), and the open circuit voltage term Vocv fitted to the polynomials for charge and discharge presented in Figure 2b with a goodness-of-fit index R^2 = 0.96. It must be noted that in considering separate V_{OCV} curves for charge and discharge and the rest of ECM parameters, an energy efficiency of 75% and associated power efficiency (according to ECM parameters) are embedded for the RT Na-S battery system in the simulations, assuming no losses from other circuitry components of the overall system, such as in-series connections and wiring.

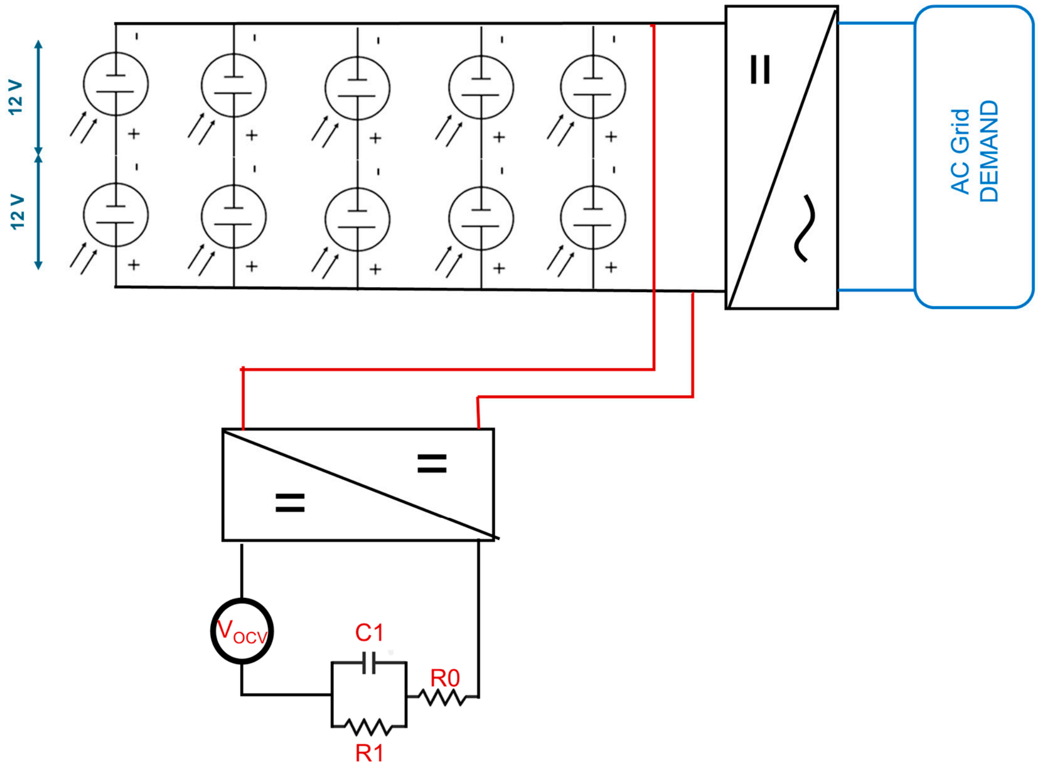

Figure 3. Diagram of the PV-Battery system connected in parallel. DC/DC converter is included between the PV and the battery systems, and a DC/AC converter is included between the PV and the household AC grid.

The PV-RT Na-S battery system–house grid was simulated for 4 consecutive days, each day inputting the PV power production profile and the household demand profile presented in Figure 1a. The initial conditions for the battery are as follows:

$$State\ of\ charge,\ SoC = 0;\ State\ of\ discharge,\ SoD = 1 \tag{2}$$

The simulation results are presented in Figure 4. On Day 1, the RT Na-S battery system is only charged by any excess PV energy, and the grid provides for any net demands not covered by the PV system (Figure 4a). At the end of Day 1 (Figure 4b), the battery has reached SoC = 75.85% and potential V_{batt} = 32.8 V. The charging C-rate varies from 0.004 C to 0.0125 C. On Day 2, the partially charged battery discharges (up to the limit of SoC = 0) on demand or is charged by any excess of PV energy up to the upper limit of V_{batt} = 39 V (Figure 4c). At the end of Day 2 (Figure 4d), the battery has reached SoC = 90.8% and V_{batt} = 26.17 V. The maximum discharging and charging C-rates are −0.166 C and 0.122 C, respectively. During Day 2, the battery started with SoC = 75.85%, initially discharged to SoC = 37.6%; thereafter, after 10.8 h in the day, there was excess of PV energy that charged the battery to its maximum voltage limit, SoC = 108% at 17.93 h, at which point the charging stopped until 19.7 h when the first need for net demand arose and was supplied by the battery which was discharged to SoC = 90.8% at the end of Day 2. No energy was supplied by the grid on Day 2; all net energy demands were covered by the battery.

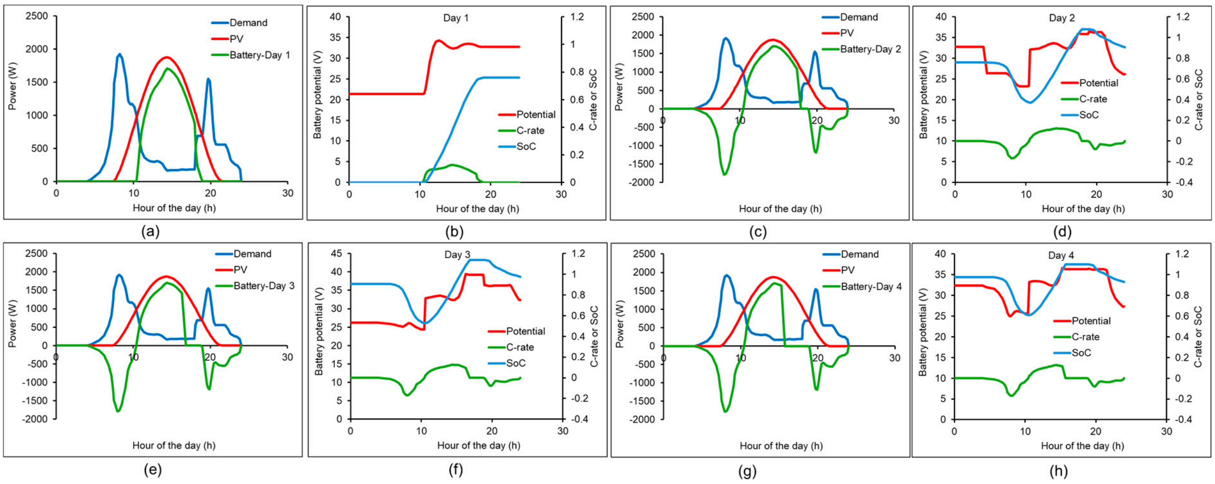

Figure 4. Simulation results of the PV-RT Na-S battery system–house grid (Figure 3) for four consecutive days: (**a**,**b**) Day 1, (**c**,**d**) Day 2, (**e**,**f**) Day 3, (**g**,**h**) Day 4.

On Day 3, the charged battery discharges (up to the limit of SoC = 0) on demand or is charged by any excess of PV energy up to the upper limit of V_{batt} = 39 V (Figure 4e). At the end of Day 3 (Figure 4f), the battery has reached SoC = 97.7% and V_{batt} = 32.4 V. The maximum discharging and charging C-rates are −0.168 C and 0.126 C, respectively. During Day 3, the battery started with SoC = 90.8%, initially discharged to SoC = 52.7%; thereafter, after 10.6 h in the day, there was excess of PV energy that charged the battery to its maximum voltage limit, SoC = 109% at 17.3 h, at which point the charging stopped until 19.9 h when the first need for net demand arose and was supplied by the battery which was discharged to SoC = 97.7% at the end of Day 3. No energy was supplied by the grid on Day 3; all net energy demands were covered by the battery.

On Day 4, the charged battery discharges (up to the limit of SoC = 0) on demand or is charged by any excess of PV energy up to the upper limit of V_{batt} = 39 V (Figure 4f). At the end of Day 4 (Figure 4g), the battery has reached SoC = 93.08% and V_{batt} = 27.3 V. The maximum discharging and charging C-rates are −0.170 C and 0.127 C, respectively. During Day 4, the battery started with SoC = 97.7%, initially discharged to SoC = 61.2%; thereafter, after 10.7 h in the day, there was excess of PV energy that charged the battery to its maximum voltage limit, SoC = 108% at 15.7 h, at which point the charging stopped until 19.9 h when the first need for net demand arose and was supplied by the battery which was discharged to SoC = 93.08% at the end of Day 4. No energy was supplied by the grid on Day 3; all net energy demands were covered by the battery.

4.2. Design and Simulations of Energy Storage Systems Integrated with the Wind Turbine System

The wind turbine system for Figure 1d is considered to be of an AC voltage of 66 kV and maximum power of 10 MW. The first case study considers a standalone RT Na-S battery pack, without any supercapacitor. The wind turbine system is connected in parallel with the RT Na-S battery pack via an AC/DC converter which translates the 66 kV AC to 42.04 V DC, which is considered to be the battery system potential. The battery system consists of 22,480 modules in series with a maximum potential of 3 V per module (to be charged to a maximum of 67,440 V) and an average potential of 1.87 V per module (system voltage of 42,037.6 V on average). For the battery system to store 16,802 kWh at a nominal system voltage of 42,037.6 V, each module needs to be of a capacity of 400 Ah. Considering a battery cell of 59 Ah (which is an assumed scaled-up version of our cell presented in Section 3.2 and Figure 2a, with the same specific capacity, energy density, power density in charge and discharge and energy efficiency), seven such cells need to be connected in parallel to form a battery module. In fact, more cells are considered to lower the C-rate; 21 cells in parallel are considered, creating 1239 Ah per battery module. Figure 2c presents the characteristic discharge–charge curves of the RT Na-S battery pack at 0.1 C and the related polynomials fitted to the experimental data. As presented in Figure 5, an AC/DC converter is connected between the wind turbine and the battery pack to control the voltage within the limits of each system, and an AC/AC converter is connected between the wind turbine and the AC grid connected with the industrial site to control the AC voltage supplied to the grid and the individual industrial site.

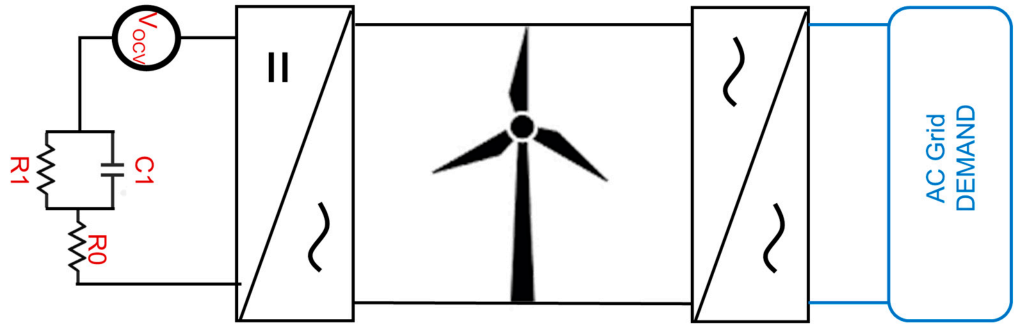

Figure 5. Diagram of the wind turbine–battery system connected in parallel. An AC/DC converter is included between the wind turbine and the battery system, and an AC/AC converter is included between the wind turbine and the industrial site AC grid.

The battery system is modeled by an equivalent circuit model (ECM) as presented in Figure 5, which consists of an in-series resistance R0 = 4.95 ohm, a Voigt element of a capacitor C1 = 87.7 mF and a resistor R1 = 5.65 ohm (from electrical impedance spectroscopy data of our RT Na-S pouch cell presented in Section 3.2 after 200 cycles at 0.1 C), and the open circuit voltage term Vocv fitted to the polynomials for charge and discharge is presented in Figure 2c with a goodness-of-fit index R^2 = 0.96. It must be noted that considering separate V_{OCV} curves for charge and discharge and the rest of ECM parameters, an energy efficiency of 75% and associated power efficiency (according to ECM parameters) are embedded for the RT Na-S battery system in the simulations, assuming no losses from other circuitry components of the overall system, such as in-series connections and wiring.

The wind turbine–RT Na-S battery system—industrial grid was simulated for 4 consecutive days, each day inputting the wind turbine power production profile and the industrial site grid demand profile presented in Figure 1c,d. The simulation results are presented in Figure 6. On Day 1, the RT Na-S battery system is only charged by any excess wind energy, and the grid provides for any net demands not covered by the wind turbine system (Figure 6a). At the end of Day 1 (Figure 6b), the battery has reached SoC = 31.8% and potential V_{batt} = 55,820 V. The charging C-rate varies from 0.004 C to 0.147 C.

On Day 2, the partially charged battery discharges (up to the limit of SoC = 0) on demand or is charged by any excess of wind turbine energy up to the upper limit of V_{batt} = 67,440 V (Figure 6c). At the end of Day 2 (Figure 6d), the battery has reached SoC = 31.24% and V_{batt} = 55,770 V. The maximum discharging and charging C-rates are −0.005 C and 0.12 C, respectively. During Day 2, the battery started with SoC = 31.8% and was charged to SoC = 52.15%; thereafter, after 8.1 h in the day, there was net demand that discharged the battery to a minimum SoC = 23.7% at 19.6 h, at which point the battery charging returned until the end of the day, after 24 h, to SoC = 31.24%. No energy was supplied by the grid on Day 2; all net energy demands were covered by the battery.

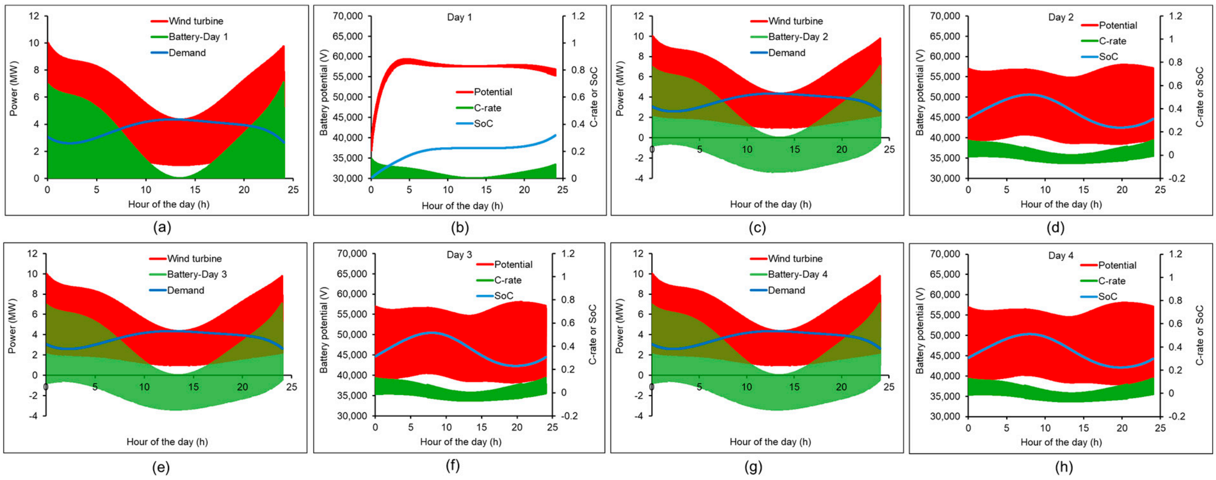

Figure 6. Simulation results of the wind turbine–RT Na-S battery system–industrial grid (Figure 5) for four consecutive days: (**a**,**b**) Day 1, (**c**,**d**) Day 2, (**e**,**f**) Day 3, (**g**,**h**) Day 4.

On Day 3, the partially charged battery discharges (up to the limit of SoC = 0) on demand or is charged by any excess of wind turbine energy up to the upper limit of V_{batt} = 67,440 V (Figure 6e). At the end of Day 3 (Figure 6f), the battery has reached SoC = 30.6% and V_{batt} = 55,740 V. The maximum discharging and charging C-rates are −0.005 C and 0.125 C, respectively. During Day 3, the battery started with SoC = 31.24% and was charged to SoC = 51.4%; thereafter, after 8.7 h in the day, there was net demand that discharged the battery to a minimum SoC = 23.05% at 19.6 h, at which point the battery charging returned until the end of the day, after 24 h, to SoC = 30.6%. No energy was supplied by the grid on Day 3; all net energy demands were covered by the battery.

On Day 4 the partially charged battery discharges (up to the limit of SoC = 0) on demand or is charged by any excess of wind turbine energy up to the upper limit of V_{batt} = 67,440 V (Figure 6g). At the end of Day 4 (Figure 6h), the battery has reached SoC = 29.9% and V_{batt} = 55,730 V. The maximum discharging and charging C-rates are −0.005 C and 0.125 C, respectively. During Day 4, the battery started with SoC = 30.6% and was charged to SoC = 50.8%; thereafter, after 8.7 h in the day, there was net demand that discharged the battery to a minimum SoC = 22.3% at 19.6 h, at which point the battery charging returned until the end of the day, after 24 h, to SoC = 29.9%. No energy was supplied by the grid on Day 4; all net energy demands were covered by the battery.

Given the large mass of the RT Na-S battery for the wind turbine system (Figure 1d), 315 tons of battery was employed in the simulations that produced the results in Figure 6 (which is equivalent to 194 m^3 of battery), a hybrid RT Na-S battery–supercapacitor system was employed in a new case study integrated with the wind system, as designed at the end of Section 3. The battery–supercapacitor system is considered with the battery and the supercapacitor connected in parallel (sharing the same maximum voltage), with a DC/DC converter between them that converts the supercapacitor voltage to the same voltage as that of the battery and the DC voltage of the AC/DC converter between the wind turbine and the battery in Figure 5. An algorithm was written for the power split between the battery and the supercapacitor (essentially current split) on the basis of the following empirical rule: when the battery C-rate exceeds a threshold (in absolute) in charge or discharge, the excess of power is stored or delivered by the supercapacitor [142]. This C-rate threshold was set at 0.1 C for both charge and discharge. As, without a supercapacitor, the C-rate in Figure 6 was above 0.1 C only in charge, the supercapacitor would take over only in charge, reaching the maximum voltage and fully charged state towards the end of Day

3. For this reason, when the battery is discharged to the grid, if the supercapacitor has sufficient charge, it is set to charge the battery at 10% of the battery discharge power.

The wind turbine–battery–supercapacitor–industrial grid system was simulated for 4 consecutive days, each day inputting the wind turbine power production profile and the industrial site grid demand profile presented in Figure 1c,d. The simulation results are presented in Figure 7. For all four days and at all times, the battery C-rate was maintained between the specified limits of −0.1 C at discharge and 0.1 C in charge, according to the power split strategy between the battery and the supercapacitor. The supercapacitor potential reached a maximum of 30.89 kV at the end of Day 1, 53.9 kV at 6.9 h on Day 2, 31.6 kV at 6.9 h on Day 3 and 31.9 V at 6.9 h on Day 4. The battery potential was 57.19 kV at the end of Day 1, 57.25 kV on Day 2, 57.14 kV on Day 3 and 57.03 kV on Day 4. Hence, the supercapacitor contributes to maintaining the battery at a steady state from one day to the next, while it maintains the battery C-rate within the specified limits. This ensures the safe operation of the RT Na-S battery. No energy was supplied by the grid on Days 2–4; all net energy demands were covered by the battery and the supercapacitor.

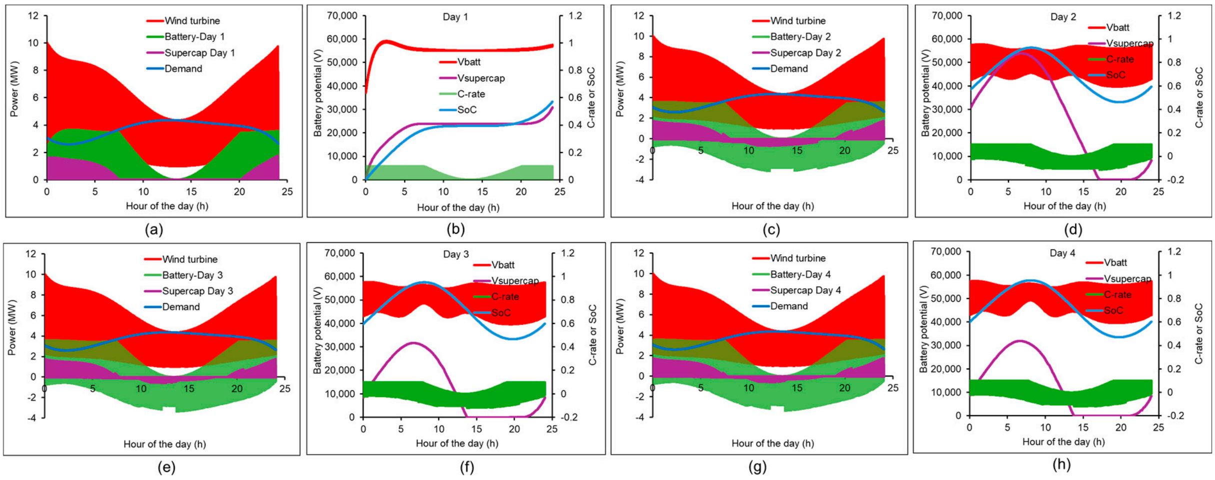

Figure 7. Simulation results of the wind turbine–RT Na-S battery system–supercapacitor–industrial grid for four consecutive days: (**a**,**b**) Day 1, (**c**,**d**) Day 2, (**e**,**f**) Day 3, (**g**,**h**) Day 4.

5. Conclusions

We have concluded that RT Na-S batteries, at an energy density of 177 Wh/kg of pouch cell and 287 Wh/L of the pouch cell and 0.1 C-rate, tested successfully in charge and discharge, have exceeded the energy density of typical LFP batteries [117–122,137,138,140], other RT Na-S batteries with data in the literature with regard to cell mass [25] and Na-ion batteries [136]. Hence, they offer great potential for high energy applications and are recommended in the present study for stationary storage: on their own for relatively low power requirements, broadly provided by the battery mass satisfying the energy requirements, as an energy storage system designed for a PV panel system, or in combination with a supercapacitor for high power pulses as an energy storage system designed for a wind turbine. However, it is recognized that further research is needed to test these new green batteries for a large number of cycles (3000–5000 cycles) and obtain data for their aging and lifetime estimation in order to pave the way for their commercialization. Furthermore, more research may be needed for the development of composite anodes [25,143] to allow operation at higher power density and C-rates above 0.1 C while eliminating the problem of dendrite formation.

This feasibility study was conducted in two design stages for the energy storage system integrated with two alternative renewables and associated power supply and demand profiles: a PV system for a household and a wind turbine for an industrial site. In the first preliminary design stage, the mass and volume of the RT Na-S battery system was determined on the basis of the battery energy and power density and the requirements in battery charge (from the renewable source) and discharge (based on the demand profile). It was concluded that a mass of 109 kg and a volume of 67 L of RT Na-S battery cells is needed for the household PV energy supply and demand profile. This is equivalent to a volume of about $0.41 \times 0.41 \times 0.41$ m^3 which seems reasonable for a household energy storage system.

In the second case study, it was concluded that a mass of 179.1 tons or 154.6 m^3 of a hybrid battery–supercapacitor system is needed for the 7.13 MW wind turbine energy supply and industrial site demand profile. This is equivalent to a cubic volume of about $5.37 \times 5.37 \times 5.37$ m^3 which may be reasonable for a 100 m blade wind turbine. A battery system footprint of 5.37×5.37 m^2 may be hosted by an industrial site and the volume of 154.6 m^3 may be distributed from a footprint of 5.37×5.37 m^2 or even larger in the underground foundations to greater height vertically along the tall tower of the wind turbine.

The second design stage proceeded to determine the energy storage system architecture in terms of the number of cells in series and in parallel and the voltage limits of the system. The RT Na-S battery was modeled by an equivalent electric circuit model which was parameterized on the basis of experimental test data for an RT Na-S battery pouch cell. It must be appreciated that for both renewable integrated energy storage systems, and especially for the large energy storage system of thousands of cells integrated with the wind turbine, well-designed thermal management and battery control systems are required, which have not been included in the simulations of this paper but would be required for a comprehensive design of a commercial system.

In each case study, the renewable energy-battery system-microgrid was simulated for four consecutive days. After charging the energy storage system on Day 1, the battery system was self-sufficient every day, charging sufficiently from the renewable energy supply and supplying all the demand needs, without any contributions from the grid to cover the demand. Regarding the battery mass for the high maximum power wind turbine system, about half of this mass was replaced by a supercapacitor system of an energy density of 10 Wh/kg, which catered for any excess power above 0.1 C in charge or discharge and also charged the battery at a very low rate during battery discharge. Simulations for four consecutive days revealed that the battery–supercapacitor system was a very good fit for the wind power supply and grid demand profiles and covered all the net demands without any contributions required from the grid. At the same time, the operation of the RT Na-S battery pack was maintained below 0.1 C, which ensured safe system operation at the minimum mass and volume of the hybrid energy storage system of the RT Na-S battery–supercapacitor.

In conclusion, the RT Na-S battery alone or combined with a supercapacitor offers a highly sustainable solution for stationary energy storage that promises to promote the exploitation of renewable energy sources to their full capacity.

Author Contributions: Conceptualization, C.L.; methodology, H.A.A., M.E. and C.L.; software, C.L.; validation, H.A.A.; formal analysis, H.A.A., M.E. and C.L.; investigation, H.A.A., M.E. and C.L.; resources, C.L.; data curation, C.L.; writing—original draft preparation, H.A.A., M.E. and C.L.; writing—review and editing, C.L.; visualization, H.A.A., M.E. and C.L.; supervision, C.L.; project administration, C.L.; funding acquisition, C.L. All authors have read and agreed to the published version of the manuscript.

Funding: This research received no external funding.

Data Availability Statement: The original contributions presented in this study are included in the article. Further inquiries can be directed to the corresponding author.

Conflicts of Interest: The authors declare no conflicts of interest.

Abbreviations

The following abbreviations are used in this manuscript:

RT	Room temperature
PV	Photovoltaic
LFP	$LiFePO_4$
BNGs	B,N doped graphene nanoplatelets
TEGDME	Tetraethylene glycol dimethyl ether
SoC, SoD	State of charge, state of discharge

References

1. Ganzer, C.; Pratama, Y.W.; Mac Dowell, N. The role and value of inter-seasonal grid-scale energy storage in net zero electricity systems. *Int. J. Greenh. Gas Control* **2022**, *120*, 103740. [CrossRef]
2. Enasel, E.; Dumitrascu, G. Storage solutions for renewable energy: A review. *Energy Nexus* **2025**, *17*, 100391. [CrossRef]
3. Razmjoo, A.; Ghazanfari, A.; Østergaard, P.A.; Jahangiri, M.; Sumper, A.; Ahmadzadeh, S.; Eslamipoor, R. Moving toward the expansion of energy storage systems in renewable energy systems—A techno-institutional investigation with artificial intelligence consideration. *Sustainability* **2024**, *16*, 9926. [CrossRef]
4. Sadhukhan, J.; Sen, S.; Randriamahefasoa, T.M.S. Framework for optimal energy storage duration for maximum-reliability renewable electricity. *Front. Energy Res.* **2024**, *12*, 1430413. [CrossRef]
5. Dodds, P.E.; Garvey, S.D. 2-Energy storage options to balance renewable electricity systems. In *Storing Energy*, 2nd ed.; with Special Reference to Renewable Energy Sources; Elsevier: Amsterdam, The Netherlands, 2022; pp. 13–33.
6. Wind Europe. Latest Wind Energy Data for Europe: Autumn 2024. 2024. Available online: https://windeurope.org/intelligence-platform/product/latest-wind-energy-data-for-europe-autumn-2024/#:~:text=12%20September%202024-,Overview,2030%20climate%20and%20energy%20targets (accessed on 11 February 2025).
7. Solar Power Europe. The Rise of Solar PV in the EU—Key Facts. Available online: https://www.solarpowereurope.org/insights/interactive-data/total-eu-27-solar-pv-capacity-a-growth-story (accessed on 11 February 2025).
8. Puertas, R.; Marti, L. Renewable energy production capacity and consumption in Europe. *Sci. Total Environ.* **2022**, *853*, 158592. [CrossRef]
9. Reiche, D.; Bechberger, M. Policy differences in the promotion of renewable energies in the EU member states. *Energy Policy* **2004**, *32*, 843–849. [CrossRef]
10. Pacesila, M.; Burcea, S.G.; Colesca, S.E. Analysis of renewable energies in European Union. *Renew. Sustain. Energy Rev.* **2016**, *56*, 156–170. [CrossRef]
11. Brodny, J.; Tutak, M. Analyzing similarities between the European Union countries in terms of the structure and volume of energy production from renewable energy sources. *Energies* **2020**, *13*, 913. [CrossRef]
12. Kozlova, M.; Overland, I. Combining capacity mechanisms and renewable energy support: A review of the international experience. *Renew. Sustain. Energy Rev.* **2022**, *155*, 111878. [CrossRef]
13. Lin, Z.; Li, D.; Zou, Y. Energy efficiency of lithium-ion batteries: Influential factors and long-term degradation. *J. Energy Storage* **2023**, *74*, 109386. [CrossRef]
14. Baboo, J.P.; Yatoo, M.A.; Dent, M.; Hojaji Najafabadi, E.; Lekakou, C.; Slade, R.; Hinder, S.J.; Watts, J.F. Exploring different binders for a $LiFePO_4$ battery, battery testing, modeling and simulations. *Energies* **2022**, *15*, 2332. [CrossRef]
15. Ahmadi, L.; Fowler, M.; Young, S.B.; Fraser, R.A.; Gaffney, B.; Walker, S.B. Energy efficiency of Li-ion battery packs re-used in stationary power applications. *Sustain. Energy Technol. Assess.* **2014**, *8*, 9–17. [CrossRef]
16. Li, K.; Tseng, K.J. Energy efficiency of lithium-ion battery used as energy storage devices in micro-grid. In Proceedings of the IECON 2015—41st Annual Conference of the IEEE Industrial Electronics Society, Yokohama, Japan, 9–12 November 2015; pp. 005235–005240.
17. Meister, P.; Jia, H.; Li, J.; Kloepsch, R.; Winter, M.; Placke, T. Best practice: Performance and cost evaluation of lithium ion battery active materials with special emphasis on energy efficiency. *Chem. Mater.* **2016**, *28*, 7203–7217. [CrossRef]
18. Ding, Y.; Cano, Z.P.; Yu, A.; Lu, J.; Chen, Z. Automotive Li-Ion batteries: Current status and future perspectives. *Electrochem. Energy Rev.* **2019**, *2*, 1–28. [CrossRef]

19. Eftekhari, A. Energy efficiency: A critically important but neglected factor in battery research. *Sustain. Energy Fuels* **2017**, *1*, 2053–2060. [CrossRef]
20. Nazari, A.; Kavian, S.; Nazari, A. Lithium-ion batteries' energy efficiency prediction using physics-based and state-of-the-art artificial neural network-based models. *J. Energy Resour. Technol.* **2020**, *142*, 102001. [CrossRef]
21. Liu, Y.; Zhang, L.; Jiang, J.; Wei, S.; Liu, S.; Zhang, W. A data-driven learning-based continuous-time estimation and simulation method for energy efficiency and coulombic efficiency of lithium ion batteries. *Energies* **2017**, *10*, 597. [CrossRef]
22. García, A.; Monsalve-Serrano, J.; Martinez-Boggio, S.; Golke, D. Energy assessment of the ageing phenomenon in Li-Ion batteries and its impact on the vehicle range efficiency. *Energy Convers. Manag.* **2023**, *276*, 116530. [CrossRef]
23. Diouf, B.; Pode, R. Potential of lithium-ion batteries in renewable energy. *Renew. Energy* **2015**, *76*, 375–380. [CrossRef]
24. Bernabeu-Santisteban, A.; Clemente, A.; Pagès, A.; Spadaro, S.; Díaz-González, F.; Trilla, L. Data granularity studies for the development of NMC Li-ion battery models. *J. Energy Storage* **2025**, *136*, 118259. [CrossRef]
25. Pampel, J.; Dor, S.; Althues, H.; Kaskel, S. Designing room temperature sodium sulfur batteries with long cycle-life at pouch cell level. *Energy Storage Mater.* **2019**, *21*, 41–49. [CrossRef]
26. Pugalendhi, K.; Natesan, B. Recent progress in tailoring transition metal cathodes for high-performance room temperature sodium–sulfur batteries. *Tungsten* **2025**, *7*, 424–455. [CrossRef]
27. Zhao, Q.; Mei, T.; Li, Y.; Lin, X.; Niu, Y.; Jiang, J.; Xu, M.; Qi, Y. Engineered sodium metal anodes: Tackling sulfur-derivative challenges for advanced sodium–sulfur batteries. *Adv. Energy Mater.* **2025**, *15*, 2404901. [CrossRef]
28. Wu, G.; Liu, T.; Lao, Z.; Cheng, Y.; Wang, T.; Mao, J.; Zhang, H.; Liu, F.; Shi, C.; Zhou, G.; et al. Optimizing s–p orbital overlap between sodium polysulfides and single-atom indium catalyst for efficient sulfur redox reaction. *Angew. Chem. Int. Ed.* **2025**, *64*, e202422208. [CrossRef]
29. Liu, Y.; Lu, S.; Weng, S.; Xu, J.; Tu, H.; Wang, Z.; Xue, J.; Liu, L.; Zhang, F.; Sun, G.; et al. Interphase-regulated room-temperature sodium-sulfur batteries enabled by a nonflammable dual-functional electrolyte. *Adv. Energy Mater.* **2025**, *15*, 2404890. [CrossRef]
30. Blázquez-Moreno, J.M.; Páez Jerez, A.L.; Tesio, A.Y.; Benítez, A.; Caballero, A. Stable long-term cycling of room-temperature sodium-sulfur batteries based on non-complex sulfurised polyacrylonitrile cathodes. *Batter. Supercaps* **2025**, *8*, e202400640. [CrossRef]
31. He, X.; Zhang, X. A comprehensive review of supercapacitors: Properties, electrodes, electrolytes and thermal management systems based on phase change materials. *J. Energy Storage* **2022**, *56*, 106023. [CrossRef]
32. Lei, C.; Fields, R.; Wilson, P.; Lekakou, C.; Amini, N.; Tennison, S.; Perry, J.; Gosso, M.; Martorana, B. Development and evaluation of a composite supercapacitor-based 12 V transient start–stop power system for vehicles: Modelling, design and fabrication scaling up. *Proc. Inst. Mech. Eng. Part A J. Power Energy* **2021**, *235*, 914–927. [CrossRef]
33. Reece, R.; Lekakou, C.; Smith, P.A.; Grilli, R.; Trapalis, C. Sulphur-linked graphitic and graphene oxide platelet-based electrodes for electrochemical double layer capacitors. *J. Alloys Compd.* **2019**, *792*, 582–593. [CrossRef]
34. Fields, F.; Lei, C.; Markoulidis, F.; Lekakou, C. The composite supercapacitor. *Energy Technol.* **2016**, *4*, 517–525. [CrossRef]
35. Chen, G.; Han, F.; Ma, H.; Li, P.; Zhou, Z.; Wang, P.; Li, X.; Meng, G.; Wei, B. High density 3D carbon tube nanoarray electrode boosting the capacitance of filter capacitor. *Nano-Micro Lett.* **2024**, *16*, 235. [CrossRef]
36. Jin, Q.; Khandelwal, M.; Kim, W. Ultrafast high-capacitance supercapacitors employing carbons derived from Al-based metal-organic frameworks. *Energy Storage Mater.* **2024**, *70*, 103464.
37. Elsehsah, K.A.A.A.; Noorden, Z.A.; Saman, N.M. Current insights and future prospects of graphene aerogel-enhanced supercapacitors: A systematic review. *Heliyon* **2024**, *10*, e37071. [CrossRef]
38. Larasati, L.D.; Supiyeva, Z.; Islam, T.; Abbas, Q. Assimilated battery electrodes for durable hybrid supercapacitors. *Materials* **2024**, *17*, 3407. [CrossRef]
39. Aznar, P.R.D.; Beltrami, M.; Longhi, M.; Ornaghi Júnior, H.L.; Zattera, A.J.; Beltrami, L.V.R. Review: Aerogel electrodes for supercapacitor application using metal additives. *J. Mater. Sci.* **2025**, *60*, 7141–7172. [CrossRef]
40. Aziz, S.B.; Aziz, D.M.; Hama, P.O.; Abdulwahid, R.T.; Sadiq, N.M.; Al-Saeedi, S.I.; Kadir, M.F.; Sangaraju, S.; Yong, J.; Woo, H.J. Unlocking high energy density and stable electric double layer capacitor derived from sustainable biodegradable polymer electrolyte based on chitosan:polyvinyl alcohol: Potassium thiocyanate:xGlycerol ($10 \leq x \leq 30$). *Results Eng.* **2025**, *27*, 106897.
41. Rajput, S.; Tyagi, V.; Sonika; Nayak, R.; Verma, S.K. Waste-derived activated carbon for supercapacitors: Current trends and future prospects. *Energy Technol.* **2025**, *13*, 2401977.
42. Choi, J.; Jung, J.C.; Jung, W. Advances in carbon xerogels: Structural optimization for enhanced EDLC performance. *Gels* **2024**, *10*, 400. [CrossRef] [PubMed]
43. Jasrotia, P.; Kumar, T. Eco-friendly supercapacitors: Key elements in a sustainable energy landscape. *ACS Symp. Ser.* **2024**, *1471*, 139–162.
44. Cai, Y.; Wei, X.; Zhang, Y.; Jin, Y.; Chen, X. Green synthesis and applications of corn stalk–derived carbon@manganese carbonate composite in energy storage. *Ionics* **2025**. [CrossRef]

45. Sharma, R.; Rana, D.S.; Kumar, S.; Singh, R.K.; Thakur, S.; Singh, D. Coconut husk waste-derived nitrogen-doped mesoporous carbon nanomaterial as an efficient and sustainable supercapacitor. *Energy Technol.* **2024**, *12*, 2400294. [CrossRef]
46. Bangera, D.N.; Sudhakar, Y.N.; Nazareth, R.A. Concrete-based energy storage: Exploring electrode and electrolyte enhancements. *RSC Adv.* **2024**, *14*, 28854–28880. [CrossRef]
47. Chavati, G.B.; Basavaraju, S.K.; Yanjerappa, A.N.; Sannaobaiah, M.B.; Muralidhara, H.B.; Venkatesh, K.; Gopalakrishna, K. Carbon sphere-infused PET CS/PET: Enhancing energy storage efficiency of vanadium flow batteries and supercapacitors. *Energy Storage* **2025**, *7*, e70217. [CrossRef]
48. Othman, K.; Mohd, M.N.; Rahman, M.Q.A.; Nor, M.H.M.; Ngadimon, K.; Sulaiman, Z. Optimizing electric double-layer capacitor charging efficiency through a parallel monitor circuit: A comparative study with lead acid batteries. *Financ. Eng.* **2025**, *3*, 117–126. [CrossRef]
49. Criollo, A.; Benavides, D.; Arévalo, P.; Minchala-Avila, L.I.; Morales-Jadan, D. Enhancing grid stability in microgrid systems with vehicle-to-grid support and EDLC supercapacitors. *Batteries* **2025**, *11*, 231.
50. de Araujo Chagas, H.; Fonseca, T.L.; Colherinhas, G. Modeling supercapacitors with integrated conductors via molecular dynamics: Optimization and impacts on energy efficiency. *J. Power Sources* **2025**, *656*, 238100. [CrossRef]
51. Efstratiadis, A.; Tegos, A.; Varveris, A.; Koutsoyiannis, D. Assessment of environmental flows under limited data availability: Case study of the Acheloos River, Greece. *Hydrol. Sci. J.* **2014**, *59*, 731–750. [CrossRef]
52. Kaldellis, J.K. Long-term analysis of hydropower's pivotal role in sustainable future of Greece. *Energies* **2025**, *18*, 2214.
53. Manikas, K.; Skroufouta, S.; Baltas, E. Simulation and evaluation of pumped hydropower storage (PHPS) system at Kastraki reservoir. *Renew. Energy* **2024**, *222*, 119888. [CrossRef]
54. Angelakis, A.N.; Baba, A.; Valipour, M.; Dietrich, J.; Fallah-Mehdipour, E.; Krasilnikoff, J.; Bilgic, E.; Passchier, C.; Tzanakakis, V.A.; Kumar, R.; et al. Water dams: From ancient to present times and into the future. *Water* **2024**, *16*, 1889. [CrossRef]
55. Drakaki, K.K.; Sakki, G.K.; Tsoukalas, I.; Kossieris, P.; Efstratiadis, A. Day-ahead energy production in small hydropower plants: Uncertainty-aware forecasts through effective coupling of knowledge and data. *Adv. Geosci.* **2022**, *56*, 155–162. [CrossRef]
56. Efstratiadis, A.; Tsoukalas, I.; Koutsoyiannis, D. Generalized storage-reliability-yield framework for hydroelectric reservoirs. *Hydrol. Sci. J.* **2021**, *66*, 580–599. [CrossRef]
57. Ruoso, A.C.; Caetano, N.R.; Oliveira Rocha, L.A. Storage gravitational energy for small scale industrial and residential applications. *Inventions* **2019**, *4*, 64. [CrossRef]
58. Pang, M.; Du, Y.; Pei, W.; Zhang, P.; Yang, J.; Zhang, L. Pumped hydro energy storage plants in China: Increasing demand and multidimensional impacts identification. *Energies* **2025**, *18*, 1801. [CrossRef]
59. Medina, J.C.L.; Zerpa, F.A.L.; Báez, S.O.P.; Morales, C.S.; Pino, C.A.M. A study of energy production in Gran Canaria with a pumped hydroelectric energy storage plant (PHES). *Sustainability* **2025**, *17*, 435. [CrossRef]
60. Bošnjaković, M.; Veljić, N.; Božič, J.T.; Muhič, S. SWOT-AHP Analysis of the importance and adoption of pumped-storage hydropower. *Technologies* **2025**, *13*, 305.
61. Dan, Y.; Chen, Q.; Li, D.; Bai, W.; Zhou, W.; Yang, A.; Yang, J. Feasibility and case studies on converting small hydropower stations to pumped storage. *Sci. Rep.* **2025**, *15*, 11011. [CrossRef]
62. Xie, Z.; Wang, Y.; Chang, J.; Guo, A.; Niu, C.; Zheng, Y.; Tian, Z. Optimal scheduling and benefit sharing of hybrid pumped storage hydropower plants with multiple operators. *Energy* **2025**, *333*, 137242. [CrossRef]
63. Budt, M.; Wolf, D.; Span, R.; Yan, J. A review on compressed air energy storage: Basic principles, past milestones and recent developments. *Appl. Energy* **2016**, *170*, 250–268. [CrossRef]
64. Wei, L.; Liu, X.; Wu, F.; Li, H.; Wu, Y.; Zhou, H. Performance analysis of a novel isobaric compressed air energy storage (CAES) system based on dual fluid. *J. Energy Storage* **2025**, *108*, 115001.
65. Gasanzade, F.; Bauer, S. Approximating coupled power plant and geostorage simulations for compressed air energy storage in porous media. *Appl. Energy* **2025**, *380*, 125070.
66. Cui, K.; Wang, C.; Liu, Z.; Fu, D.; Chen, G.; Li, W.; Nie, L.; Shen, Y.; Xu, Y.; Kuang, R. Efficiency analysis of ocean compressed air energy storage system under constant volume air storage conditions. *Energy* **2025**, *329*, 136531. [CrossRef]
67. Zhang, Y.; Wang, H.; Jin, P.; Cai, X.; Du, J.; Zhang, W.; Wang, H.; Li, R.; Cheng, Z. Design and thermodynamic performance analysis of a novel adiabatic compressed air energy storage system based on liquid piston re-pressurization. *J. Energy Storage* **2025**, *105*, 114675. [CrossRef]
68. Zhang, L.; Xie, M.; Ye, K.; Li, S.; Chen, L. Compressed air energy storage based on variable-volume air storage: A review. *J. Energy Storage* **2025**, *110*, 115361. [CrossRef]
69. Parameshwaran, R.; Kalaiselvam, S.; Harikrishnan, S.; Elayaperumal, A. Sustainable thermal energy storage technologies for buildings: A review. *Renew. Sustain. Energy Rev.* **2012**, *16*, 2394–2433. [CrossRef]
70. Jayaprakash, V.; Ganesan, S.; Beemkumar, N.; Sunil Kumar, M.; Kamakshi Priya, K.; Kaliappan, N. Enhancing thermal energy storage efficiency: Synthesis and analysis of hybrid Nano-PCMs. *Results Eng.* **2025**, *26*, 104899. [CrossRef]

71. Wang, J.; Zhang, B.; Zhu, C.; Li, Z.; Gao, T.; Zhang, W.; Xu, C.; Ju, X. Optimal scheduling of distributed energy system in the industrial park based on pumped thermal energy storage (Carnot battery). *J. Energy Storage* **2025**, *110*, 115278. [CrossRef]
72. Liang, Z.; Zheng, G.; Wu, G.; Pan, Z.; Hu, Z.; Xu, M.; Chen, H. Thermodynamic performance of organic rankine cycle based pumped thermal energy storage system with different working fluids. *Heliyon* **2025**, *11*, e41052. [CrossRef]
73. Tetteh, M.; Li, L.; Minnick, M.; Zhou, H.; Ye, Z. Optimization of borehole thermal energy storage systems using a genetic algorithm. *Math. Geosci.* **2025**, *57*, 1–22.
74. Wang, C.; Yao, S.; Chen, X.; Yan, X.; Zhan, X. Thermal performance analysis of arc-shaped fins of horizontal latent heat thermal energy storage system. *Int. J. Heat Fluid Flow* **2025**, *112*, 109748. [CrossRef]
75. Orlić, M.; Paklar, G.B.; Džoić, T.; Jelić, P.L.; Međugorac, I.; Mihanović, H.; Muslim, S.; Pasarić, M.; Pasarić, Z.; Stanešić, A. Wind-driven upwelling in the Adriatic Sea: Coastal vs. open-sea processes. *Prog. Oceanogr.* **2025**, *234*, 103470. [CrossRef]
76. Ortega, M.; Rubinetti, S.; Konyssova, G.; Mayer, B.; Sánchez, E.; Gutiérrez, C.; Wiltshire, K.H.; Sidorenko, V. Future Wind conditions in the German Bight under RCP8.5 emissions scenario (2006–2099) from regional coupled ocean–atmosphere model system MPIOM-REMO. *Int. J. Climatol.* **2025**, *45*, e8814. [CrossRef]
77. Bhattacharya, S.; Nikitas, G. 8-Wind energy: Status and outlook with focus on offshore wind. In *Energy and Climate Change*; Elsevier: Amsterdam, The Netherlands, 2025; pp. 197–224.
78. Chen, Y.-S.; Hu, C.-Y.; Li, C.-Y.; Lin, J.-B.; Shih, Y.-C. Marine Spatial Planning for Offshore Wind Firms: A comparison of global existing policies and data for energy system storage. *Sustainability* **2025**, *17*, 5884. [CrossRef]
79. Alkhalidi, M.; Al-Dabbous, A.; Al-Dabbous, S.; Alzaid, D. Evaluating the accuracy of the ERA5 model in predicting wind speeds across coastal and offshore region. *J. Mar. Sci. Eng.* **2025**, *13*, 149. [CrossRef]
80. Barnabei, V.F.; Ancora, T.C.M.; Conti, M.; Castorrini, A.; Delibra, G.; Corsini, A.; Rispoli, F. A multi-objective optimization framework for offshore wind farm design in deep water seas. In Proceedings of the ASME Turbo Expo 2024: Turbomachinery Technical Conference and Exposition, London, UK, 24–28 June 2024; Paper No: GT2024-126008, V013T37A012. p. 12. [CrossRef]
81. Cosseron, A.; Schlosser, C.A.; Gunturu, U.B. Characterization of the wind power resource in Europe and its intermittency. *Energy Procedia* **2014**, *34*, 58–66. [CrossRef]
82. Ji, B.; Chen, C.; Zhong, K.; Xu, H.; Yin, X.; Ye, F. CFD simulation and wind loads evaluation on wind turbine blades in mountainous terrain under thunderstorm downbursts. *Int. J. Green Energy* **2025**, *22*, 3234–3254. [CrossRef]
83. Wang, W.; Chen, F. Wind field modeling over hilly terrain: A review of methods, challenges, limitations, and future directions. *Appl. Sci.* **2025**, *15*, 10186. [CrossRef]
84. Zengler, C.P.; Troldborg, N.; Gaunaa, M. Predicting the impact of flow field acceleration on wind turbine performance in complex terrain and wind farms. *J. Phys. Conf. Ser.* **2025**, *3016*, 012003. [CrossRef]
85. Biswas, S.; Chen, J.S.-J. Power coefficient for large wind turbines considering wind gradient along height. *Energies* **2025**, *18*, 740. [CrossRef]
86. Gunturu, U.B.; Schlosser, C.A. *Characterization of Wind Power Resource in the United States and Its Intermittency*; MIT JPSPGC Report 209; MIT: Cambridge, MA, USA, 2011; p. 65.
87. Kumar, R.; Rutgersson, A.; Asim, M.; Routray, A. Understanding wind characteristics over different terrains for wind turbine deployment. *Meteorol. Appl.* **2025**, *32*, e70079. [CrossRef]
88. Han, S.; Song, W.; Yan, J.; Zhang, N.; Wang, H.; Ge, C. Integrating intra-seasonal oscillations with numerical weather prediction for 15-day wind power forecasting. *IEEE Trans. Power Syst.* **2025**, *40*, 4033–4047. [CrossRef]
89. Wang, P.; Guo, J.; Cheng, F.; Gu, Y.; Yuan, F.; Zhang, F. A MPC-based load frequency control considering wind power intelligent forecasting. *Renew. Energy* **2025**, *244*, 122636. [CrossRef]
90. Wu, X.; Zhang, L.; Feng, G.; Shang, W.; Xiong, X. Capacity configuration strategy of SOEC- battery based hybrid energy storage system for suppressing fluctuation of wind power. *Proc. Inst. Mech. Eng. Part A J. Power Energy* **2025**, *239*, 599–606. [CrossRef]
91. Matayoshi, H.; Mitsuhashi, M.; Onoe, R.; Morizane, T.; Furukakoi, M.; Senjyu, T. A novel higher rotational speed maintaining control for wind power generation systems under unstable wind conditions. *Green Technol. Sustain.* **2025**, *3*, 100113. [CrossRef]
92. Lv, Z.-C.; Wang, P.-F.; Wang, J.-C.; Tian, S.-H.; Yi, T.-F. Key challenges, recent advances and future perspectives of rechargeable lithium-sulfur batteries. *J. Ind. Eng. Chem.* **2023**, *124*, 68–88. [CrossRef]
93. Fei, Y.; Li, G. Unveiling the pivotal parameters for advancing high energy density in lithium-sulfur batteries: A comprehensive review. *Adv. Funct. Mater.* **2024**, *34*, 2312550. [CrossRef]
94. Grabe, S.; Dent, M.; Zhang, T.; Tennison, S.; Lekakou, C. A physicochemical model-based digital twin of Li–S batteries to elucidate the effects of cathode microstructure and evaluate different microstructures. *J. Power Sources* **2023**, *580*, 233470. [CrossRef]
95. Dent, M.J.; Grabe, S.; Hinder, S.J.; Masteghin, M.G.; Whiting, J.D.; Watts, J.F.; Lekakou, C. A step-by-step design strategy to realize high-performance lithium–sulfur batteries. *ACS Appl. Energy Mater.* **2025**, *8*, 1492–1506. [CrossRef] [PubMed]
96. Wang, X.; Guo, Y.; Chen, D.; Hou, Y.; He, Q.; Gao, X.; Ye, Z.; Zhang, Q.; Lu, J. Carbonaceous sulfur host for cathodes in room-temperature metal–sulfur batteries. *ACS Energy Lett.* **2024**, *9*, 3093–3135.

97. Marri, I.; Edfouf, Z.; Caballero, A.; Tesio, A.Y. Valorisation of argan seeds: Production of cathode material for high-performance lithium-sulphur batteries. *J. Energy Storage* **2024**, *82*, 110518. [CrossRef]
98. Joseph, H.M.; Fichtner, M.; Munnangi, A.R. Perspective on ultramicroporous carbon as sulphur host for Li–S batteries. *J. Energy Chem.* **2021**, *59*, 242–256. [CrossRef]
99. Han, W.; Li, Q.; Zhu, H.; Luo, D.; Qin, X.; Li, B. Hierarchical porous graphene bubbles as host materials for advanced lithium sulfur battery cathode. *Front. Chem.* **2021**, *9*, 653476. [CrossRef]
100. Ye, X.; Ruan, J.; Pang, Y.; Yang, J.; Liu, Y.; Huang, Y.; Zheng, S. Enabling a stable room-temperature sodium–sulfur battery cathode by building heterostructures in multichannel carbon fibers. *ACS Nano* **2021**, *15*, 5639–5648. [CrossRef]
101. Hueso, K.; Armand, M.; Rojo, T. High temperature sodium batteries: Status, challenges and future trends. *Energy Environ. Sci.* **2013**, *6*, 734–749. [CrossRef]
102. Nikiforidis, G.; van de Sanden, M.C.M.; Tsampas, M.N. High and intermediate temperature sodium–sulfur batteries for energy storage: Development, challenges and perspectives. *RSC Adv.* **2019**, *9*, 5649–5673. [CrossRef] [PubMed]
103. Vudata, S.P.; Bhattacharyya, D. Thermal management of a high temperature sodium sulphur battery stack. *Int. J. Heat Mass Transf.* **2021**, *181*, 122025. [CrossRef]
104. Jeevarajan, J.A.; Joshi, T.; Parhizi, M.; Rauhala, T.; Juarez-Robles, D. Battery hazards for large energy storage systems. *ACS Energy Lett.* **2022**, *7*, 2725–2733. [CrossRef]
105. Gao, Z.; Yang, S.; Chen, R.; Ding, Y.; Guo, S.; Zhan, S.; Cui, B.; Zheng, J.; Liu, T.; Luo, H.; et al. Multiscale failure mechanisms and safety assessment of commercial sodium-ion batteries. *Adv. Funct. Mater.* **2025**, e07323. [CrossRef]
106. Zhu, Z.; Jiang, T.; Ali, M.; Meng, Y.; Jin, Y.; Cui, Y.; Chen, W. Rechargeable batteries for grid scale energy storage. *Chem. Rev.* **2022**, *122*, 16610–16751. [CrossRef]
107. Gupta, A.; Suhag, S. Evaluation of energy storage systems for sustainable development of renewable energy systems—A comprehensive review. *J. Renew. Sustain. Energy* **2022**, *14*, 032702. [CrossRef]
108. Arellano-Prieto, Y.; Chavez-Panduro, E.; Rossi, P.S.; Finotti, F. Energy storage solutions for offshore applications. *Energies* **2022**, *15*, 6153. [CrossRef]
109. Adeoye, H.A.; Dent, M.; Watts, J.F.; Tennison, S.; Lekakou, C. Solubility and dissolution kinetics of sulfur and sulfides in electrolyte solvents for lithium–sulfur and sodium–sulfur batteries. *J. Chem. Phys.* **2023**, *158*, 064702. [CrossRef]
110. Marangon, V.; Barcaro, E.; De Boni, F.; Prato, M.; Bresser, D.; Hassoun, J. Effective liquid electrolytes for enabling room-temperature sodium–sulfur batteries. *Adv. Sustain. Sys.* **2024**, *8*, 2400268. [CrossRef]
111. Guo, D.; Wang, J.; Lai, T.; Henkelman, G.; Manthiram, A. Electrolytes with solvating inner sheath engineering for practical Na–S batteries. *Adv. Mater.* **2023**, *35*, 2300841. [CrossRef] [PubMed]
112. Wu, J.; Tian, Y.; Gao, Y.; Gao, Z.; Meng, Y.; Wang, Y.; Wang, X.; Zhou, D.; Kang, F.; Li, B.; et al. Rational electrolyte design toward cyclability remedy for room-temperature sodium–sulfur batteries. *Angew. Chem. Int. Ed.* **2022**, *61*, e202205416. [CrossRef]
113. Sungjemmenla; Vineeth, S.K.; Yamauchi, Y.; Kumar, V. Chapter: Electrolytes for room-temperature sodium-sulfur batteries: A holistic approach to understand solvation. In *Room-Temperature Sodium-Sulfur Batteries*, 1st ed.; CRC Press: Boca Raton, FL, USA, 2023.
114. Tian, L.; Yang, Z.; Yuan, S.; Milazzo, T.; Cheng, Q.; Rasool, S.; Lei, W.; Li, W.; Yang, Y.; Jin, T.; et al. Designing electrolytes with high solubility of sulfides/disulfides for high-energy-density and low-cost K-Na/S batteries. *Nat. Comm.* **2024**, *15*, 7771. [CrossRef]
115. Kumar, A.; Ghosh, A.; Forsyth, M.; MacFarlane, D.R.; Mitra, S. Free-radical catalysis and enhancement of the redox kinetics for room-temperature sodium−sulfur batteries. *ACS Energy Lett.* **2020**, *5*, 2112–2121. [CrossRef]
116. Adeoye, H.A.; Tennison, S.; Watts, J.F.; Lekakou, C. An investigation into electrolytes and cathodes for room-temperature sodium–sulfur batteries. *Batteries* **2024**, *10*, 216. [CrossRef]
117. White, C.; Swan, L.G. Pack-level performance of electric vehicle batteries in second-life electricity grid energy services. *J. Energy Storage* **2023**, *57*, 106265. [CrossRef]
118. Fan, T.; Liang, W.; Guo, W.; Feng, T.; Li, W. Life cycle assessment of electric vehicles' lithium-ion batteries reused for energy storage. *J. Energy Storage* **2023**, *71*, 108126. [CrossRef]
119. Thakur, J.; de Almeida, C.M.L.; Baskar, A.G. Electric vehicle batteries for a circular economy: Second life batteries as residential stationary storage. *J. Clean. Prod.* **2022**, *375*, 134066. [CrossRef]
120. Carvalho, M.L.; Temporelli, A.; Girardi, P. Life cycle assessment of stationary storage systems within the Italian electric network. *Energies* **2021**, *14*, 2047. [CrossRef]
121. Wang, Y.; Tang, B.; Shen, M.; Wu, Y.; Qu, S.; Hu, Y.; Feng, Y. Environmental impact assessment of second life and recycling for LiFePO4 power batteries in China. *J. Environ. Manag.* **2022**, *314*, 115083. [CrossRef]
122. Zhang, M.; Wang, L.; Wang, S.; Ma, T.; Jia, F.; Zhan, C. A critical review on the recycling strategy of lithium iron phosphate from electric vehicles. *Small Methods* **2023**, *7*, 2300125. [CrossRef] [PubMed]
123. Fu, A.; Wang, C.; Pei, F.; Cui, J.; Fang, X.; Zheng, N. Recent advances in hollow porous carbon materials for lithium–sulfur batteries. *Small* **2019**, *15*, 1804786. [CrossRef] [PubMed]

124. Dent, M.; Grabe, S.; Ayere, O.; Babar, S.; Masteghin, M.G.; Cox, D.C.; Howlin, B.J.; Baker, M.A.; Lekakou, C. Investigating PEDOT: PSS binder as an energy extender in sulfur cathodes for Li–S batteries. *ACS Appl. Energy Mater.* **2024**, *7*, 7349–7361. [CrossRef]
125. Baboo, J.P.; Jakubczyk, E.; Yatoo, M.A.; Phillips, M.; Grabe, S.; Dent, M.; Hinder, S.J.; Watts, J.F.; Lekakou, C. Investigating battery-supercapacitor material hybrid configurations in energy storage device cycling at 0.1 to 10C rate. *J. Power Sources* **2023**, *561*, 232762. [CrossRef]
126. Li, Z.; Sami, I.; Yang, J.; Li, J.; Kumar, R.V.; Chhowalla, M. Lithiated metallic molybdenum disulfide nanosheets for high-performance lithium–sulfur batteries. *Nat. Energy* **2023**, *8*, 84–93. [CrossRef]
127. Wasim, M.S.; Habib, S.; Amjad, M.; Bhatti, A.R.; Ahmed, E.M.; Qureshi, M.A. Battery-ultracapacitor hybrid energy storage system to increase battery life under pulse loads. *IEEE Access* **2022**, *10*, 62173–62182. [CrossRef]
128. Çorapsiz, M.R.; Kahveci, H. A study on Li-ion battery and supercapacitor design for hybrid energy storage systems. *Energy Storage* **2023**, *5*, e386. [CrossRef]
129. Yi, Z.; Zhao, K.; Sun, J.; Wang, L.; Wang, K.; Ma, Y. Prediction of the remaining useful life of supercapacitors. *Math. Probl. Eng.* **2022**, *2022*, 7620382. [CrossRef]
130. Vermisoglou, E.C.; Giannouri, M.; Todorova, N.; Giannakopoulou, T.; Lekakou, C.; Trapalis, C. Recycling of typical supercapacitor materials. *Waste Manag. Res.* **2016**, *34*, 337–344.
131. Bou-Rabee, M.A.; Sulaiman, S.A.; Choe, G.; Han, D.; Saeed, T.; Marafie, S. Characteristics of solar energy radiation on typical summer and winter days in Kuwait. *Int. J. Automot. Mech. Eng.* **2015**, *12*, 2944–2953. [CrossRef]
132. Koudouris, G.; Dimitriadis, P.; Iliopoulou, T.; Mamassis, N.; Koutsoyiannis, D. Investigation on the stochastic nature of the solar radiation process. *Energy Procedia* **2017**, *125*, 398–404. [CrossRef]
133. Sandelic, M.; Sangwongwanich, A.; Blaabjerg, F. Reliability evaluation of PV systems with integrated battery energy storage systems: DC-coupled and AC-coupled configurations. *Electronics* **2019**, *8*, 1059.
134. De Kooning, J.D.M.; Meersman, B.; Vandoorn, T.L.; Vandevelde, L. Evaluation of the maximum power point tracking performance in small wind turbines. In Proceedings of the 2012 IEEE Power and Energy Society General Meeting, San Diego, CA, USA, 22–26 July 2012. [CrossRef]
135. Kumar, P.; Bansal, S.; Sonthalia, A. Chapter 4—Introduction to battery systems. In *Handbook of Thermal Management Systems*; Aloui, F., Varuvel, E.G., Sonthalia, A., Eds.; Elsevier: Amsterdam, The Netherlands, 2023; p. 97.
136. Abraham, K.M. How comparable are sodium-ion batteries to lithium-ion counterparts? *ACS Energy Lett.* **2020**, *5*, 3544–3547. [CrossRef]
137. Napolskiy, F.; Avdeev, M.; Yerdauletov, M.; Ivankov, O.; Bocharova, S.; Ryzhenkova, S.; Kaparova, B.; Mironovich, K.; Burlyaev, D.; Krivchenko, V. On the use of carbon nanotubes in prototyping the high energy density Li-ion batteries. *Energy Technol.* **2020**, *8*, 2000146. [CrossRef]
138. Chandra, G.; Kashyap, S.J.; Sreedhara, S.S.; Bulusu, S.V.; Ananthula, V.V.; Vijay, R.; Rao, T.N.; Srinivasan, A. Enhanced stability and high-yield LiFePO4/C derived from low-cost iron precursors for high-energy Li-ion batteries. *J. Energy Storage* **2023**, *72*, 108453. [CrossRef]
139. Yang, X.-G.; Liu, T.; Wang, C.-Y. Thermally modulated lithium iron phosphate batteries for mass-market electric vehicles. *Nat. Energy* **2021**, *6*, 176–185. [CrossRef]
140. Gorsch, J.; Schneiders, J.; Frieges, M.; Kisseler, N.; Klohs, D.; Heimes, H.; Kampker, A.; Castro, M.M.; Siebecke, E. Contrasting a BYD Blade prismatic cell and Tesla 4680 cylindrical cell with a teardown analysis of design and performance. *Cell Rep. Phys. Sci.* **2025**, *6*, 102453. [CrossRef]
141. Zhao, R.; Liu, J.; Ma, F. Cathode chemistries and electrode parameters affecting the fast charging performance of Li-ion batteries. *J. Electrochem. Energy Convers. Storage* **2020**, *17*, 021111. [CrossRef]
142. Santucci, A.; Sorniotti, A.; Lekakou, C. Power split strategies for hybrid energy storage systems for vehicular applications. *J. Power Sources* **2014**, *258*, 395–407. [CrossRef]
143. Eren, E.O.; Esen, C.; Scoppola, E.; Song, Z.; Senokos, E.; Zschiesche, H.; Cruz, D.; Lauermann, I.; Tarakina, N.V.; Kumru, B.; et al. Microporous sulfur–carbon materials with extended sodium storage window. *Adv. Sci.* **2024**, *11*, 2310196. [CrossRef] [PubMed]